J Adv Ceram

Research Article

Stabilizing high-entropy MAX phases by incorporating tin

Lei Cao[1], Xinghua Zhu[1], Shuai Fu[2], Detian Wan[2], Yiwang Bao[3], Yanchun Zhou[4,✉], Man Jiang[1], Longsheng Chu[1], Qingguo Feng[1], Chunfeng Hu[1,✉]

Cite this article: Cao L, Zhu X, Fu S, et al. *J Adv Ceram* 2025, **14**(2): 9221028. https://doi.org/10.26599/JAC.2025.9221028

ABSTRACT: High-entropy nanolaminated materials, referred to as MAX phases, have exceptional potential in various fields, including physics, mechanics, and energy storage, owing to their diverse compositions and outstanding properties. However, synthesizing stable high-entropy phases presents significant challenges because of the considerable differences in the physical and chemical properties of complex elements. In this study, we added low-melting-point metal tin (Sn) as an additive to facilitate the formation of solid solutions. The cohesion energy and formation enthalpy of the Sn-containing system are negative, which maintains the thermodynamic stability of the system, and the incorporation of Sn decreases the mixing enthalpy of the target high-entropy MAX phase and inhibits the formation of competing phases. The addition of Sn increases the lattice parameter and improves the structural stability by increasing the lattice distortion of octahedral M_6X and prism M_6A, which facilitates the successful synthesis of single-phase high-entropy MAX bulk materials. In addition, the high-entropy MAX phases with added Sn retain good mechanical and physical properties. This study provides a novel approach for the synthesis and application of high-entropy MAX phase materials, which has the potential to contribute to advancements in multiple technological fields.

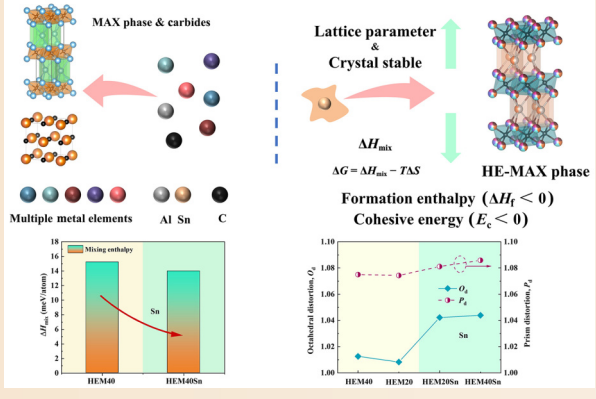

KEYWORDS: high-entropy MAX phase; low melting-point metal tin; first-principles calculations; structural distortion; properties

1 Introduction

High-entropy materials represent a promising class characterized by the combination of multiple principal metallic elements into a single phase, driven by configurational entropy [1,2]. Unlike traditional solid solutions, high-entropy materials do not require a dominant element. This characteristic allows for a broad range of compositions, facilitating advancements in diverse applications, including physics, mechanical property analysis, energy storage, and energy conversion [3]. While high-entropy alloys initially led the way in this field, recent developments have underscored the potential of high-entropy ceramics in applications such as thermal protection, rechargeable batteries, wear-resistant coatings, and catalysis [4–6]. Despite these advantages, the incorporation of multiple elements introduces complexity to its synthetics.

At high temperatures, competing phases may exhibit lower free energy due to a small entropy change, making the formation of single-phase structures challenging. Conversely, at room temperature, the lower mixing enthalpy of competing phases can lead to phase separation. Additionally, significant differences in ionic radii complicate the formation of single-phase high-entropy compounds, affecting lattice stability and leading to challenges in phase transitions. The nearly equiatomic distribution of elements complicates the application of classical predictive criteria such as Hume-Rothery and Vegard's laws [7]. New methods, including atomic size differences [8], valence electron concentration (VEC) [9], and root-mean-square (RMS) analysis [10], are emerging to better predict and understand the stability of high-entropy materials. The results indicate that as the number of elements increases, both the structure and phase change, leading to the development of phenomenological criteria to guide the synthesis of high-entropy materials. For example, minimal lattice distortion is observed in the quaternary alloy FeCoNiCr. However, upon the addition of palladium (Pd) to form the FeCoNiCrPd alloy, notable lattice distortion becomes apparent [11].

High-entropy engineering has significantly advanced the development of MAX phase materials defined by the formula $M_{n+1}AX_n$, which consists of an early transition metal (M), an A-group element (A), and carbon, nitrogen, or boron (X) [12,13]. The high-entropy MAX phase and its derived MXene have been

[1] Key Laboratory of Advanced Technologies of Material, Ministry of Education, School of Material Science and Engineering, Southwest Jiaotong University, Chengdu 610031, China. [2] State Key Laboratory of Green Building Material, China Building Material Academy, Beijing 100024, China. [3] Henan Key Laboratory of High Performance Carbon Fiber Reinforced Composites, Institute of Carbon Matrix Composites, Henan Academy of Sciences, Zhengzhou 450046, China. [4] School of Material Science and Engineering, Zhengzhou University, Zhengzhou 450001, China.

✉ Corresponding authors. E-mail: Y. Zhou, yczhou@alum.imr.ac.cn; C. Hu, chfhu@live.cn

Received: October 7, 2024; Revised: December 13, 2024; Accepted: January 3, 2025

shown to have promising applications in a number of areas, including high-temperature friction components, absorbent materials, and energy storage facilities [14–18]. Although the thermodynamic stability of high-entropy MAX phases has been predicted by density functional theory (DFT) calculations [19], many challenges remain in investigating their physical and mechanical properties as structural materials, particularly the frequent occurrence of a second phase during the synthesis process [20–22].

An effective approach for controlling the formation of multiphase products in high-entropy systems is low-melting-point metal-assisted synthesis. This method has been successful in the production of materials such as MoB and GaN, with Si *et al.* [23], Chen *et al.* [24], and Cao *et al.* [25] demonstrating its efficacy in generating single-phase high-entropy alloys and oxides. During the synthesis process, low-melting-point metals facilitate the diffusion of atoms and the homogenization of components, which is particularly beneficial in high-entropy materials. The liquid-phase environment accelerates the diffusion of atoms with different radii, compensating for their slow diffusion rates and promoting the formation of a homogeneous solid solution. Moreover, the addition of a low-melting-point metal reduces the mixing enthalpy, leading to a decrease in the Gibbs free energy for the target product, thereby suppressing the formation of competing phases.

On the other hand, Ye *et al.* [10] and He *et al.* [26] demonstrated that structural stability is crucial for the synthesis of a single-phase high-entropy material. They noted that a solid solution comprising multiple atoms with significant radius differences can lead to lattice distortions, and these distorted lattices may exhibit greater stability than ideal lattices by releasing the elastic distortion energy induced by atomic and modulus differences. Thus, achieving stable distorted lattices is key to ensuring the successful synthesis of a single-phase high-entropy material. Hug *et al.* [27] defined the distortion degree of octahedral M_6X and trigonal M_6A structures in relation to ideal hexagonal close-packed (HCP) structures via octahedral distortion (O_d) and prism distortion (P_d) parameters. They reported that the modulation of A-site elements not only triggers changes in the octahedral M_6X and prism M_6A structures but also affects the modulus properties of the material. The addition of the low-melting-point metal tin has been to be an effective method for the synthesis of single-phase S-containing high-entropy MAX phases, promoting the structural stability of the material by optimizing the lattice distortion and energy release [28].

This study investigated a novel approach to synthesizing single-phase high-entropy MAX phases on the basis of the 211 structure (M_2AlC) using low-melting-point tin (Sn) as an additive while elucidating its underlying mechanisms. Through a combination of theoretical calculations and experimental analysis, the effects of Sn addition on key thermodynamic parameters, including the mixing enthalpy, formation enthalpy, and cohesive energy, as well as the relationship between lattice parameter adjustments and the lattice distortion induced by the Sn solid solution, were systematically examined. These findings reveal that Sn reduces the mixing enthalpy to ensure thermodynamic stability and increases the distortion of the M_6X and M_6A structures, facilitating the release of elastic strain energy. These factors collectively enable the stable synthesis of single-phase high-entropy MAX phases from thermodynamic and structural perspectives. Moreover, this study evaluated the impact of a Sn solid solution on the physical and mechanical properties of MAX phases and demonstrated that Sn-containing high-entropy MAX phase ceramics maintain outstanding overall performance. Therefore, this work offers new theoretical perspectives and methodological strategies for advancing the synthesis and application of high-entropy MAX phases.

2 Experimental

2.1 Sample preparation

Commercial titanium (Ti), vanadium (V), niobium (Nb), tantalum (Ta), hafnium (Hf), aluminum (Al), tin (Sn), and graphite powders (purity 99.9%, 500 mesh; ENO High-Tech Material Development Co., Ltd., China) were mixed via ball milling at a speed of 50 r/min for 10 h. The ratio of balls to materials was 2 : 1, and the balls occupied approximately half of the milling tank volume. Agated balls were employed as grinding material, with the ratio of large balls to small balls set at 2 : 1. Additionally, the milling tank was filled with argon gas to maintain an inert atmosphere throughout the process. The powder compositions were designed according to the molar ratios of the following formulas: Formula 1: Ti : V : Nb : Ta : Hf : Al : C = 0.45 : 0.45 : 0.45 : 0.45 : 0.2 : 1.1 : 0.95, abbreviated as HEM20; Formula 2: Ti : V : Nb : Ta : Hf : Al : Sn : C = 0.45 : 0.45 : 0.45 : 0.45 : 0.2 : 0.55 : 0.55 : 0.95, abbreviated as HEM20Sn; Formula 3: Ti : V : Nb : Ta : Hf : Al : Sn : C = 0.4 : 0.4 : 0.4 : 0.4 : 0.4 : 0.55 : 0.55 : 0.95, abbreviated as HEM40Sn. Excessive elements were added to the A-site primarily because of volatility, whereas the amount of graphite intentionally remained low, as carbon defects can stabilize most aluminum-containing MAX phases [29]. The mixed powders were consolidated in a spark plasma sintering (SPS) furnace (SPS-20T-10, Chenhua Technology Co., Ltd., China) with a heating rate of 50 °C/min under an argon atmosphere at 30 MPa. The high-entropy MAX phases were sintered at 1370 °C for 20 min and then naturally cooled to ambient temperature. Finally, contaminants on the surface of the graphite foil were removed via a diamond grinding wheel.

2.2 Characterizations

The phase compositions of the HEM20, HEM20Sn, and HEM40Sn samples were analyzed via an X-ray diffractometer (XRD; Ultima IV, Rigaku, Japan). The Archimedes method was employed to determine the densities of the samples. The fracture and etched surfaces of the synthesized samples were observed via a field emission scanning electron microscope (FE-SEM; Apreo 2C, FEI, USA). The sample surfaces were polished to a mirror finish, followed by chemical etching using a solution composed of HNO_3, HCl, and H_2O in a 1 : 1 : 1 volume ratio. Backscattered electron (BSE) images were used to analyze the grain size. More than 100 grains were counted to ensure statistical reliability. The elements were analyzed via an energy dispersion spectroscope (EDS; ULTIM Max65, Oxford, UK). Transmission electron microscope (TEM; Talos F200S G2, FEI, USA) was used to characterize the morphology and element distribution of the particles. Powders for TEM analysis were prepared by drilling directly from the bulk ceramics. The extracted powders were ultrasonically dispersed in ethanol to ensure uniform distribution. A copper grid was used to collect the dispersed particles, and particles of similar sizes were carefully selected for observation. The coefficient of thermal expansion (CTE) of each sample was measured via a thermal expansion analyzer (NETZSCH DIL 402C, Selb, Germany). The measurements were conducted in an argon atmosphere with a heating rate of 10 °C/min, covering a temperature range from room temperature to 1200 °C. The CTE was determined via a bar sample with dimensions of 4 mm ×

4 mm × 15 mm. The thermal conductivity (λ) of the samples was calculated via Eq. (1):

$$\lambda = \sigma \cdot c_p \cdot \rho \quad (1)$$

where σ represents the thermal diffusivity (mm²/s), c_p represents the heat capacity (J/(g·K)), and ρ represents the density (g/cm³). The specific heat capacity (c_p) was measured via the reference standard method with graphite as the reference material. c_p of the sample was determined by comparing its thermal response with that of graphite, which has a known specific heat capacity under identical testing conditions. The measurements were carried out using a cylindrical sample with dimensions of ϕ12.5 mm × 2 mm in a laser thermal conductivity meter (NETZSCH LFA467, Selb, Germany).

The Vickers hardness was measured via a Vickers hardness tester (HVS-50, Lianer Co., China) under load 9.8 N with a dwell time of 15 s. The flexural strength, fracture toughness, and compressive strength of the samples were tested. The measurement of flexural strength was based on the standard of ISO 14704:2000, and the evaluation of fracture toughness corresponded to the standard of ISO 15732:2033. The flexural strength was measured using a sample with dimensions of 1.5 mm × 2 mm × 18 mm. Fracture toughness was measured via the single-edge notched beam (SENB) method with samples 2 mm × 4 mm × 18 mm in size, featuring a notch length of 2 mm and a width of 0.2 mm. The specimens for the compressive strength test had dimensions of 2 mm × 2 mm × 4 mm. The tests were conducted via an electronic universal testing machine (YC-100KN, Oneyice Co., China) with crosshead speeds of 0.5 mm/min for flexural strength and compressive strength testing and 0.05 mm/min for fracture toughness testing. The span was set at 16 mm, and for each test, five samples were used.

2.3 Model computing

This work is based on DFT implemented in the Vienna *ab initio* simulation package (VASP) [30]. Special quasirandom structures (SQS) of high-entropy MAX models generated by the alloy theoretic automated toolkit (ATAT) were utilized for this calculation [31]. All the models were 5 × 2 × 2 supercells containing 160 atoms. Three SQS models were used for each component to obtain reliable statistical averages.

The Perdew–Burke–Ernzerhof (PBE) exchange-correlation functional and projector augmented-wave (PAW) pseudopotential were utilized in this work [32,33]. A cutoff energy of 550 eV was employed to compute all the models. The self-consistent field (SCF) convergence threshold was set to 1×10^{-5} eV/atom. All the models were optimized for atomic positions, ensuring that the force on each ion was less than 0.02 eV/Å. Spin polarization was considered in all the models, and a 2 × 4 × 1 *k*-point grid in the Brillouin zone was applied for all the calculations. Program VASPKIT was employed for the analysis of the density of states (DOS) [34], whereas visualization for electronic and structural analysis (VESTA) [35] was used to generate the electron localization function (ELF) [36]. Convergence test results were included in the Electronic Supplementary Material (ESM).

3 Results and discussion

3.1 Synthesis strategy

Figure 1(a) illustrates the synthesis strategy for the high-entropy MAX phase. The formation of a second phase typically occurs when M-site transition metal elements are introduced in equal proportions to the five groups of elements (Ti/Nb/V/Ta/Hf). However, the addition of Sn not only provides a favorable liquid-phase environment for diffusion but also occupies the A-site, increasing the lattice parameter and enhancing the crystal stability. Additionally, the presence of Sn slightly reduces the mixing enthalpy, resulting in a negative enthalpy of formation and cohesive energy, thereby promoting the synthesis of a single-phase high-entropy MAX phase both thermodynamically and structurally. The experimental results from the XRD patterns shown in Fig. S1 in the ESM indicate that comparing $(TiVNbTa)_2AlC$ (denoted as MMAX) with $(TiVNbTaHf)_2AlC$ (denoted as HEM40) confirms that the addition of Hf directly causes separation of the high-entropy MAX phase (see the ESM).

Figure 1(b) depicts the atomic radius disparity and conformational entropy data for the M sites in the MAX phases: quaternary medium-entropy MMAX, nonisotropic high-entropy HEM20, and isotropic high-entropy HEM40. The atomic radius difference (δ) is calculated via Eq. (2) [8]:

$$\delta = \sqrt{\sum_{i=1}^{n} x_i (1 - r_i/r)^2} \quad (2)$$

where n is the total number of elements, x_i is the concentration of the ith element, r_i is the radius of the ith component element, and r is the average radius. The configurational entropy (ΔS_{conf}) is calculated via Eq. (3) [4]:

$$\Delta S_{conf} = -R \sum_{i=1}^{n} x_i \ln x_i \quad (3)$$

where R is the molar gas constant, n is the total number of elements, and x_i is the concentration of the ith element. δ was calculated on the basis of the atomic radii with relevant data referenced from Ref. [37]. δ values and ΔS_{conf} values for the M-site (Wyckoff site 4*f*) in MMAX, HEM20, and HEM40 are calculated to be 2.94%, 4.00%, and 4.61%, respectively, with corresponding entropy values of 1.39*R*, 1.57*R*, and 1.61*R*. The δ values and ΔS_{conf} values of the A-site (Wyckoff site 2*d*) with Sn added are 7.41% and 0.69*R*, respectively [38]. As the complexity of the components increases, the conformational entropy also increases, following this trend. The figure illustrates that the nonisotropic HEM20 exhibits a conformational entropy exceeding 1.50*R*, aligning with the conventional assessment of high-entropy compounds. Notably, HEM20 can directly synthesize single-phase high-entropy MAX phases, which is essential for investigating the structural features and property changes associated with the solid solution of Sn.

Figure 1(c) presents a perspective view of the SQS model for HEM40 and HEM40Sn along the *a*-axis direction of the crystal, which is utilized for DFT calculations. The other three models, MMAX, HEM20Sn, and HEM20, are constructed via the same methodology. Importantly, all the models employed in this study consisted of 160 atoms, and detailed model information can be found in Fig. S3 in the ESM.

Figure 1(d) shows the theoretical variation in the lattice constants (*a* and *c*). The lattice constants for both *a* and *c* axes notably increase with the formation of solid solutions containing Hf and Sn. This trend contrasts with that observed in single-component MAX-phase material. For example, experimental findings for $Zr_2Al_{(1-x)}Sn_xC$ and $Ti_2Al_{(1-x)}Sn_xC$ revealed that the solid solution of Sn primarily increased the lattice constant of the *a*-axis while having a negligible effect on the *c*-axis [39,40]. However, in this study, the addition of Sn resulted in a significant increase in the *c*-axis lattice constant for both HEM20 and HEM20Sn. This suggests that the interactions between the solid

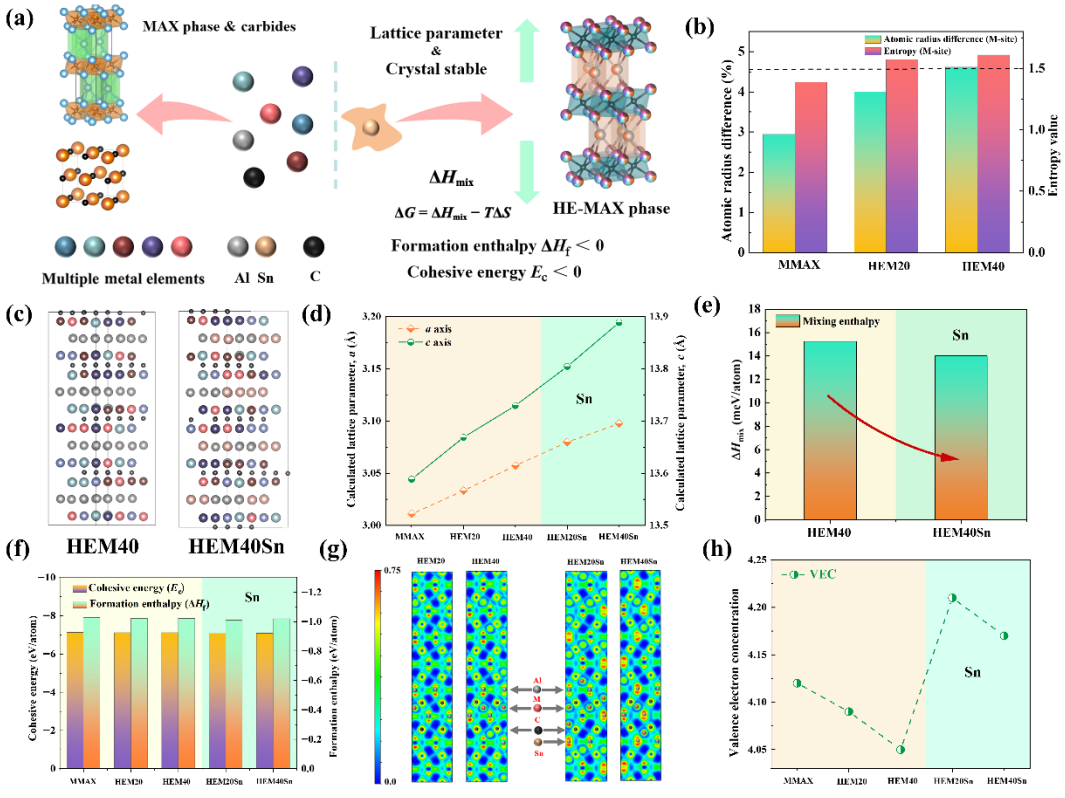

Fig. 1 Schematic diagram of high-entropy single-phase MAX phase block synthesis strategy. (a) Overview of high-entropy MAX phase synthesis; (b) atomic radius differences and conformational entropy (M-site) for MMAX, HEM20, and HEM40; (c) SQS models of HEM40 and HEM40Sn; (d) theoretically calculated lattice parameters for MMAX, HEM20, HEM40, HEM20Sn, and HEM40Sn; (e) mixing enthalpy of HEM40 and HEM40Sn; (f) heat of formation and cohesive energy for MMAX, HEM20, HEM40, HEM20Sn, and HEM40Sn; (g) ELF maps for HEM20, HEM40, HEM20Sn, and HEM40Sn along [100] direction; (h) valence electron concentration for MMAX, HEM20, HEM40, HEM20Sn, and HEM40Sn.

solutions of multiple transition metals at the M-site and Sn in the A-layer are more complex, leading to a substantial increase in the *c*-axis lattice constant and a larger volume of the crystal cell. This finding will be verified experimentally, where it will be shown that the solid solution of the larger-sized Hf atom is favored.

Figure 1(e) shows the calculations of the enthalpy of mixing for HEM40 and HEM40Sn. The enthalpy of mixing is determined via data from the carbide high-entropy ceramics (Eqs. (4) and (5)) [41,42]:

$$\Delta H_{mix} = E_{HEM} - (E_{Hf_2AlC} + E_{Ta_2AlC} + E_{Nb_2AlC} + E_{Ti_2AlC} + E_{V_2AlC}) \quad (4)$$

$$\Delta H_{mix}\,(Sn) = E_{HEMSn} - (E_{Hf_2AlSnC} + E_{Ta_2AlSnC} + E_{Nb_2AlSnC} + E_{Ti_2AlSnC} + E_{V_2AlSnC}) \quad (5)$$

As illustrated in the figure, the mixing enthalpy of HEM40Sn is slightly lower than that of HEM40 upon the addition of Sn. In accordance with the Gibbs free energy equation ($\Delta G = \Delta H_{mix} - T\Delta S$), a reduction in the mixing enthalpy (ΔH_{mix}) can contribute to a decrease in the Gibbs free energy of the system and prevent competing phase generation. Moreover, the entropy of mixing for HEM40Sn is closer to zero, indicating that the different elements in the system can be randomly distributed, which contributes to a more stable solid solution phase in the solid-state [27]. To further substantiate the unique role of Sn at the A-site, comparative experiments were conducted using Ge, a high-melting-point A-site element. Attempts to synthesize a single-phase high-entropy MAX phase with Ge were unsuccessful (see XRD results in Fig. S2 in the ESM). This provides additional evidence of Sn's distinctive role at the A-site, as it not only enhances the entropy effect but also facilitates the stable formation of a single-phase high-entropy MAX phase.

Figure 1(f) illustrates the enthalpy of formation and cohesive energy for MMEX, HEM20, HEM40, HEM20Sn, and HEM40Sn. The enthalpy of formation indicates the thermodynamic stability of the material, whereas the cohesive energy reflects the interaction forces between atoms within the solid. Both parameters are crucial indicators of the overall thermodynamic stability of material. Structural stability is a key consideration in DFT calculations. Therefore, in this work, the energy of cohesion (E_c) and enthalpy of generation (ΔH_f) of the HEM40 and HEM40Sn MAX phases are calculated compared with those of the high-entropy MAX phase. The energy of cohesion (E_c) and enthalpy of generation (ΔH_f) can be calculated via Eqs. (6) and (7) [43,44]:

$$E_{c\text{-}HEM} = E_{total}^{HEM} - \left(l_1 E_{iso}^{Hf} + l_2 E_{iso}^{Ti} + l_2 E_{iso}^{Nb} + l_2 E_{iso}^{V} + l_2 E_{iso}^{Ta} + m E_{iso}^{Al/Sn} + n E_{iso}^{C}\right) \quad (6)$$

$$\Delta H_{f\text{-}HEM} = \frac{1}{l_1 + 4l_2 + m + n}\left[E_{total}^{HEM} - (l_1 E_{bulk}^{Hf} + l_2 E_{bulk}^{Ti} + l_2 E_{bulk}^{Nb} + l_2 E_{bulk}^{V} + l_2 E_{bulk}^{Ta} + m E_{bulk}^{Al/Sn} + n E_{bulk}^{C})\right] \quad (7)$$

where $E_{c\text{-}HEM}$, $\Delta H_{f\text{-}HEM}$, and E_{total}^{HEM} represent the cohesive energy, the formation enthalpy, and the total energy for HEM40 and HEM40Sn MAX phase compounds, respectively. E_{iso} and E_{bulk} are the energies per atom of the constituent elements (M, Al/Sn, and C) in the isolated and bulk states, respectively. The letters *l*, *m*,

and n represent the number of M elements, Al/Sn, and C atoms in the unit cell, respectively. Specifically, due to differences in formulations, the atomic count of Hf may differ from those of the other four M elements. Therefore, in the formula, the atomic count of Hf is denoted by l_1, while the atomic counts of the four M elements are collectively represented by l_2. As illustrated in the figure, the enthalpy of generation and cohesion energy of the five MAX phases are less than zero and exhibit similar values, indicating that these high-entropy MAX phases are thermodynamically stable. This finding provides further confirmation that the solid solution of Sn has no significant effect on the synthesis or stability of the material.

Figure 1(g) presents the ELF plots for HEM20, HEM40, HEM20Sn, and HEM40Sn, with values ranging from 0.0 to 0.75. In these plots, colors closer to red indicate a higher degree of electron localization, whereas colors closer to blue represent stronger electron delocalization [43,44]. For HEM20 and HEM40, which have different percentages of elemental Hf at the M-site, the ELF diagrams do not show significant differences. However, when Sn partially substitutes Al, a notable change occurs: the degree of electron localization around Sn is greater than that around Al. This suggests a more concentrated electron distribution between Sn and the surrounding atoms, which may lead to stronger covalent interactions. These properties are expected to positively influence the stability of the crystal structures in high-entropy MAX phases. The models and detailed data utilized for the calculations in Fig. 1 can be found in Figs. S3 and S4 and Tables S1–S4 in the ESM. Figure S5 in the ESM shows that the projected density of states (PDOS) of each element at the M site with Sn and Al indicates that Sn is more electronically localized than Al with the transition elements at the M position, forming high-entropy crystal structures with stronger bonding energies that can stabilize severe lattice distortions.

Figure 1(h) depicts the valence electron concentration profiles of MMEX, HEM20, HEM40, HEM20Sn, and HEM40Sn. The valence electron concentrations of all five MAX phases are observed to fall within the range of 4.0–4.25. Notably, Sn has a valence electron count of 4, higher than Al (3), making it the element with the highest electron count in the system under consideration [45]. The valence electron concentrations of HEM20Sn and HEM40Sn are greater than those in systems without solidified Sn. Zhou *et al.* [46] investigated the valence electron concentrations of the MAX and MAB phases in relation to elasticity constants to predict the formation of new phases and their properties. These findings indicate that the valence electron concentration of the MAX phase typically ranges from 3.75 to 5.00. Additionally, the bulk modulus (B) increases with increasing valence electron concentration, whereas the shear modulus (G) tends to decrease. This trend is also supported by the data for the HEM20Sn and HEM40Sn systems presented in this study.

3.2 Microstructure characterizations

Figure 2(a) presents the XRD patterns of the synthesized samples compared with the ICDD PDF card (No. 97-060-6258), revealing a typical 211 structure. Notably, a shift in the XRD patterns for HEM20Sn and HEM40Sn, relative to HEM20, is observed upon the addition of Sn and Hf. This shift is attributed to the larger atomic radius of Sn (1.45 Å) than of Al (1.25 Å), whereas Hf has the largest atomic radius among the M-site elements at 1.55 Å [37]. Additionally, the figure indicates that the intensity of the (002) peak decreases as Sn dissolves into the A-site, a trend that is consistent with prior research [39,40]. This reduction in peak intensity has also been observed in single-component MAX phases when Sn is incorporated into the A-site. The disordered arrangement of elements affects the diffraction intensity [47]. Lapauw *et al.* [48] reported a decrease in the relative XRD

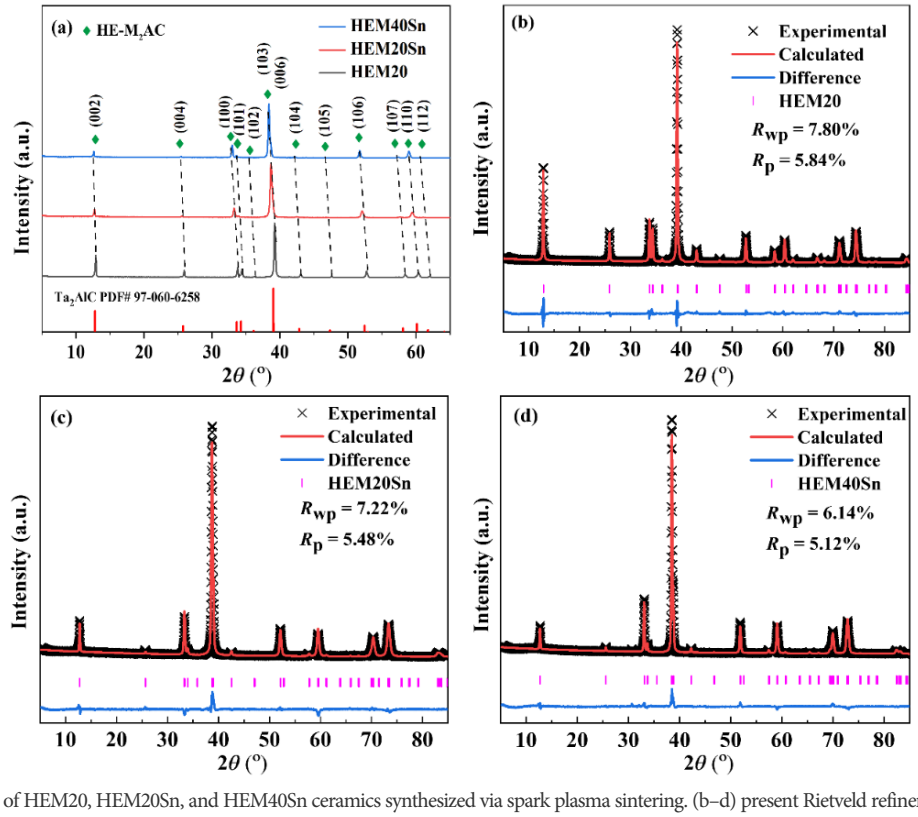

Fig. 2 (a) XRD patterns of HEM20, HEM20Sn, and HEM40Sn ceramics synthesized via spark plasma sintering. (b–d) present Rietveld refinement of XRD patterns for high-entropy ceramics: (b) HEM20, (c) HEM20Sn, and (d) HEM40Sn.

intensity for multicomponent MAX phases, attributing this effect to distortions that influence X-ray dispersion.

The Rietveld refinement (Figs. 2(b)–2(d)) offers more detailed lattice parameters for HEM20, HEM20Sn, and HEM40Sn. While the complex elemental environment of high-entropy materials may introduce some uncertainty, semiquantitative discussions regarding the effects of high-entropy MAX phases and Sn substitution remain valid. The lattice parameters and atomic positions of the samples were refined via FullProf.2k (Version 7.95-Jan2023-ILL JRC) software. The goodness of fit was evaluated by weighted residual variance factor (R_{wp}) and residual variance factor (R_p) with the fitting results yielding reliability coefficients of R_{wp} = 7.80%, 7.22%, and 6.14% and R_p = 5.84%, 5.48%, and 5.12% for HEM20, HEM20Sn, and HEM40Sn, respectively.

Table 1 presents the lattice constants, Wyckoff positions, and parameters of the fitting results of the three samples. The lattice parameters of HEM20, HEM20Sn, and HEM40Sn are as follows: a = 3.067 Å, c = 13.759 Å; a = 3.107 Å, c = 13.880 Å; a = 3.127 Å, c = 13.939 Å, respectively, and the absolute value of the c-axis clearly increased. In prior studies examining the solid solutions of Sn and Al within the A site of single-component MAX phases, the addition of Sn led to an expansion of the lattice parameters along the a-axis, whereas the c-axis showed minimal changes [39,40]. However, this result contrasts with the findings of the current study on high-entropy MAX phases, where both the a-axis and the c-axis exhibited notable changes, particularly with the solid solutions of Hf and Sn.

Hug *et al.* [27] examined the deviation of the MAX phase (211) structure from the ideal HCP structure. They described the degree of distortion by calculating the structures of the octahedral M_6X and the trigonal prism M_6A. Their findings highlighted the importance of this distortion in stabilizing the MAX phase. Recent studies on high-entropy materials also suggest that lattice distortion from the ideal structure plays a key role in overall stability. In an ideal 211 crystal structure, which is represented by closely packed spheres with identical radii, both deformation parameters are set to 1, and the theoretical c/a ratio is approximately 4.89, whereas the standard Z_M position is approximately 1/12, which is approximately 0.0833. The octahedral distortion, referred to as O_d, is measured by the ratio of distances between opposite faces of the octahedron. The lattice parameters a and c and the internal position Z_M of the 211 MAX phase can be calculated via Eq. (8) [27]:

$$O_d = \frac{d_1}{d_2} = \frac{\frac{\sqrt{3}}{2}a}{\sqrt{4(Z_M c)^2 + \frac{a^2}{12}}} = \frac{\sqrt{3}}{2\sqrt{4Z_M^2\left(\frac{c}{a}\right)^2 + \frac{1}{12}}} \quad (8)$$

where d_1 is the distance between planes deviating from the basal plane, and d_2 is between planes parallel to the basal plane. Similarly, the distortion P_d of M_6A trigonal prisms can be calculated by the ratio of the atomic distances d_{M-M} and d_{M-A} via the calculation formulas for a, c, and Z_M (Eq. (9)) [49]:

$$P_d = \frac{d_{M-M}}{d_{M-A}} = \frac{1}{\sqrt{\frac{1}{3} + \left(\frac{1}{4} - Z_M\right)^2\left(\frac{c}{a}\right)^2}} \quad (9)$$

Figure 3 illustrates how the lattice parameters vary with different alloying elements and concentrations. In Fig. 3(a), the schematic of the 211 MAX phase structure highlights the importance of M_6X octahedra and M_6A trigonal prisms, which are the essential structural units influencing the overall distortion in the MAX phase. In the image, the projection of the M_6X structure along the b-axis (with the a-axis perpendicular to the viewing plane) forms a parallelogram, with d_1 and d_2 as adjacent sides. Owing to the presence of Sn and Al in the outer A-layers of the M_6X structure, along with the unequal bonding strengths of the Sn and Al with the M atoms, the parallelogram undergoes distortion. This results in an increase in the O_d distortion parameter. Figure 3(b) shows the O_d and P_d values for HEM20, HEM40, HEM20Sn, and HEM40Sn. In the samples without Sn, both HEM40 and HEM20 exhibit similar P_d and O_d values, with HEM20 displaying slightly lower distortion than HEM40. This suggests that the addition of Hf requires an increase in both O_d and P_d to stabilize the structure. Furthermore, the HEM40 sample contains approximately 23 wt% carbides, whereas HEM20 reaches its solubility limit [25].

With the addition of Sn, both O_d and P_d increase significantly in HEM20Sn, indicating that this increase in distortion reduces the free energy, facilitating the dissolution of more Hf into the M-site. This observation is supported by the results of HEM40Sn, where O_d does not significantly increase, implying that the distortion introduced by Sn in the M_6X structure is sufficient to alleviate the strain caused by Hf solubility. In contrast to O_d, the P_d of HEM40Sn continues to rise, suggesting that Hf's solubility at the M-site primarily impacts the M_6X structure, whereas the insertion of the A-layer requires additional distortion in M_6A to release elastic strain energy.

Figures 3(c) and 3(d) display changes in the lattice constants (c-axis and a-axis), c/a ratio, and Z_M, illustrating structural distortions due to shifts in the lattice parameters. Compared with those of HEM40, both the a-axis and c-axis of HEM20 slightly decrease, which can be attributed to Hf having the largest atomic radius among the five transition metals. With the addition of Sn, the a-axis and c-axis of HEM20Sn increase significantly, with the change in the c/a ratio being largely driven by atomic radius effects. Previous studies have shown that Sn addition to the A-site

Table 1 Lattice parameters, atomic positions, and refinement results of HEM20, HEM20Sn, and HEM40Sn ceramics

Formula (unit cell)	HEM40 [22]	HEM20	HEM20Sn	HEM40Sn
Space group	$P6_3/mmc$ (#194)	$P6_3/mmc$ (#194)	$P6_3/mmc$ (#194)	$P6_3/mmc$ (#194)
Unit-cell dimension	$a = b$ = 3.075 Å, c = 13.776 Å	$a = b$ = 3.067 Å, c = 13.759 Å	$a = b$ = 3.106 Å, c = 13.880 Å	$a = b$ = 3.127 Å, c = 13.939 Å
M	4*f* (1/3,2/3,0.08985)	4*f* (1/3,2/3,0.09016)	4*f* (1/3,2/3,0.08718)	4*f* (1/3,2/3,0.08724)
Al	2*d* (1/3,2/3,3/4)	2*d* (1/3,2/3,3/4)	2*d* (1/3,2/3,3/4)	2*d* (1/3,2/3,3/4)
C	2*a* (0.0,0.0,0.0)	2*a* (0.0,0.0,0.0)	2*a* (0.0,0.0,0.0)	2*a* (0.0,0.0,0.0)
R_p	6.10	5.84	5.48	5.12
R_{wp}	8.63	7.80	7.22	6.14
R_{exp}	2.73	2.81	2.97	2.87
Chi-square	10.0	7.71	5.91	4.59

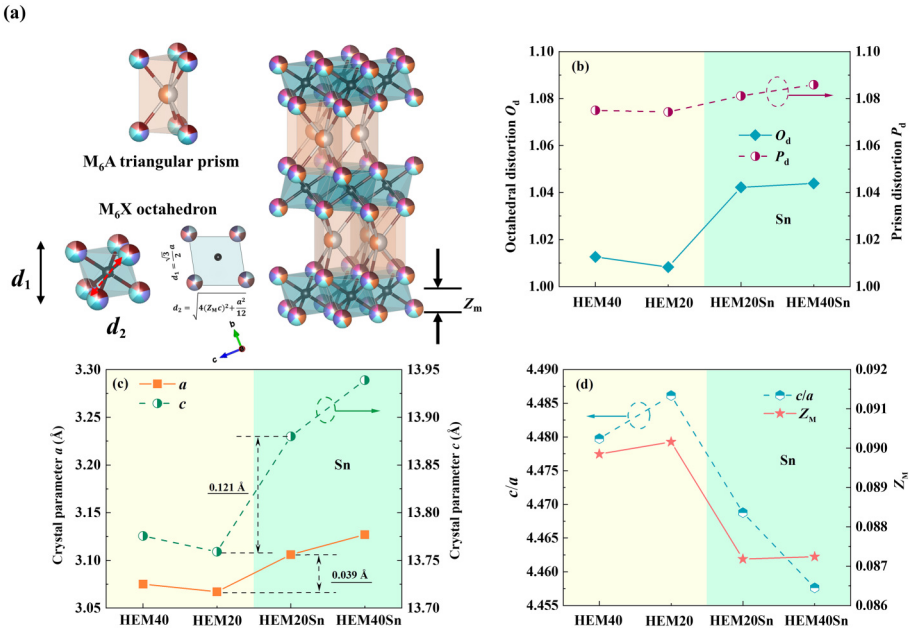

Fig. 3 Variation in crystal structure with composition. (a) Schematic structure of 211 MAX phase, (b) O_d and P_d, (c) *a* and *c* parameters, and (d) *c*/*a* ratio and internal free parameter Z_M. The data of HEM40 are taken from Ref. [22].

primarily increases the *a*-axis, with minor changes in the *c*-axis. DFT calculations indicate that the increase in the *c*-axis of H_2SnC is less than 0.1 Å compared with that of H_2AlC, implying that this effect results from the combined influence of multiple transition metals at the M-site and interactions between Sn and Al at the A-site [50,51].

Furthermore, the change in the internal free parameter Z_M is affected primarily by Sn solubility, with only a minimal difference observed between HEM40Sn and HEM20Sn. Overall, the distortion of O_d and P_d plays a key role in facilitating the solubility of elements at the M site. When the M site cannot generate enough distortion on its own, the addition of elements such as Sn at the A site helps increase both O_d and P_d distortions, increasing the solubility of M-site elements. This further increases P_d distortion, contributing to the stabilization of the overall crystal structure.

SEM and EDS were used to characterize and analyze the element distribution, grain morphology, and fracture features of three high-entropy MAX phases. Figures 4(a)–4(c) correspond to the nominal compositions of HEM20, HEM20Sn, and HEM40Sn, respectively. The compositional maps obtained from the polished surface EDS confirmed a uniform distribution of all the elements in the HE-MAX phase at the micrometer scale, with no significant compositional segregation observed. The black dots observed in the image are identified as pores and alumina (Al_2O_3), which are commonly found in MAX phases containing Al at the A-site [52,53]. Figure S7 in the ESM shows secondary electron and backscattered electron images, along with EDS at the corresponding locations for detailed characterization. Furthermore, minimal interference from typical carbides and intermetallic compounds occurs. TEM and EDS were utilized to analyze the composition of the particles, as shown in Figs. 4(d)–4(f). The elemental mapping images obtained through TEM demonstrated a uniform distribution of all elements within the grains, indicating that there was no significant compositional segregation. This finding confirms the formation of a homogeneous solid solution throughout the system. Figures 4(g)–4(i) depict the fracture surface images of the samples HEM20, HEM20Sn, and HEM40Sn, with insets providing magnified views of the fracture faces and corresponding element spectra. The EDS results for regions 1–3 are included, with the elemental contents of the samples listed in Table 2. Owing to limitations in accurately representing the carbon (C) content, EDS was used primarily for qualitative analysis. The ratio of elements at the M-site to the A-site is approximately 2 : 1, which is consistent with the composition ratio of 211 MAX phases, further confirming that the synthesized products are indeed high-entropy 211 MAX phases.

As presented in Table 2, the entropy values for HEM20, HEM20Sn, and HEM40Sn are 1.561*R*, 1.565*R*, and 1.602*R*, respectively, all exceeding the threshold of 1.50*R* defined for high-entropy materials. These three samples meet the criteria for five-element configurations at the M site and exhibit entropy values that align with the characteristics of high-entropy MAX phases. The properties of high-entropy MAX phases are discussed in the following section. The relative densities of the samples were calculated on the basis of the EDS mapping results (Fig. S6 and Table S5 in the ESM). The measured densities of HEM20, HEM20Sn, and HEM40Sn are 7.14, 8.23, and 8.56 g/cm^3, respectively, whereas their theoretical densities are 7.31, 8.24, and 8.91 g/cm^3, respectively. The calculated relative densities are 97.67%, 99.87%, and 96.07%, respectively.

The chemically etched polished surfaces are shown in Figs. 4(j)–4(l). The average grain sizes of the HEM20, HEM20Sn, and HEM40Sn ceramics were measured to be approximately 4.36, 15.92, and 12.28 μm in length and 2.00, 4.55, and 3.60 μm in width, respectively. In comparison, the grain sizes of single-component MAX phases typically fall within the range of 13–20 μm [54–56]. High-entropy materials typically exhibit smaller grain sizes due to the suppression of atomic diffusion caused by the incorporation of atoms with different sizes and lattice distortion. In samples containing Sn, a liquid phase forms above 230 °C when Sn liquefies and persists until it is completely dissolved into the A-site. The presence of this liquid phase effectively wets the solid particles, reduces the interfacial energy, and enhances contact diffusion between particles, thereby improving the sintering kinetics.

Furthermore, the high mobility of the liquid phase facilitates materials diffusion and redeposition, significantly accelerating the

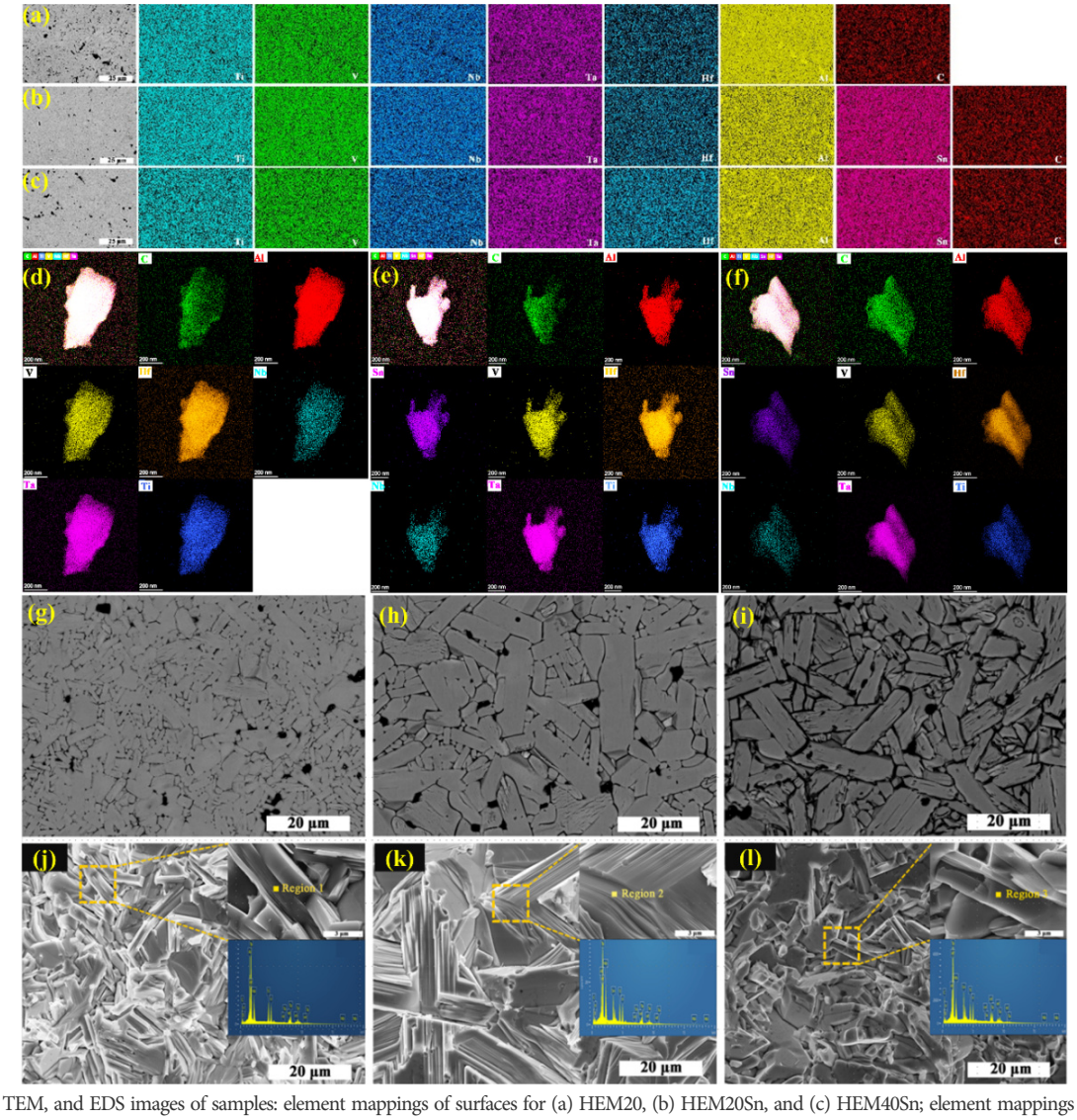

Fig. 4 SEM, TEM, and EDS images of samples: element mappings of surfaces for (a) HEM20, (b) HEM20Sn, and (c) HEM40Sn; element mappings of particles for (d) HEM20, (e) HEM20Sn, and (f) HEM40Sn; polish etching images for (g) HEM20, (h) HEM20Sn, and (i) HEM40Sn; micromorphological images and composition analysis for (j) HEM20, (k) HEM20Sn, and (l) HEM40Sn.

Table 2 Compositions (at%) and calculated entropies at the M-site of HEM20, HEM20Sn, and HEM40Sn ceramics based on EDS analysis

Region	Ceramic	Ti	V	Nb	Ta	Hf	Al	Sn	C	Entropy (M)
1	HEM20	5.87	4.73	5.09	6.96	2.46	11.35	—	63.55	1.561*R*
2	HEM20Sn	6.24	5.59	7.10	5.73	2.60	6.89	6.25	59.61	1.565*R*
3	HEM40Sn	4.66	4.55	4.16	5.38	5.76	4.76	5.81	64.92	1.602*R*

grain growth process. As a result, samples containing Sn have larger grain sizes. For the HEM40Sn ceramics, the M site has a greater entropy due to the isoatomic ratio, which results in a smaller grain size than that of the HEM20Sn ceramics. This is mainly due to lattice distortion and atom size differences, which increase the grain boundary energy, thereby hindering grain boundary migration and suppressing grain growth.

3.3 Physical properties

Figure 5 shows the thermal expansion curves of high-entropy MAX phases in an argon atmosphere over a temperature range of 25–1200 °C. These curves represent the actual thermal expansion behavior of the samples HEM20, HEM20Sn, and HEM40Sn, with the red lines indicating the linear fitting results based on the temperature function. According to the fitting results, the calculated average CTEs for samples HEM20, HEM20Sn, and HEM40Sn are 9.46×10^{-6}, 9.08×10^{-6}, and 9.54×10^{-6} K^{-1}, respectively (The fitting equations are provided in Fig. S8 in the ESM). These values are comparable to those of other single-phase MAX materials, which range from 8×10^{-6} to 10×10^{-6} K^{-1}. The phenomenon of thermal expansion occurs due to the increase in the kinetic energy of particles within a material when subjected to rising temperatures. In solids, atoms oscillate around their equilibrium positions, and an increase in temperature results in larger amplitudes of vibration.

As a result of the existing interatomic forces, the increased vibration leads to a greater average distance between atoms, which manifests macroscopically as an expansion of the volume. Compared with HEM20Sn and HEM40Sn, the addition of Sn does not significantly change the thermal expansion coefficients of

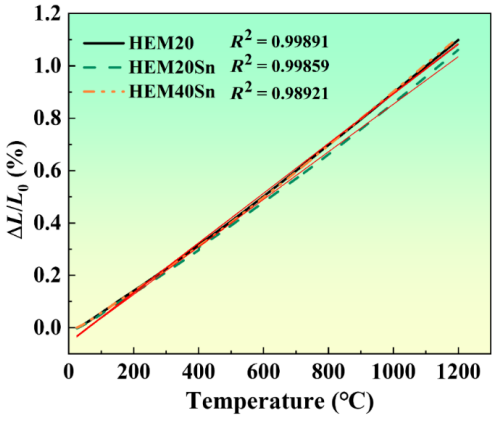

Fig. 5 Temperature-dependent thermal expansion of HEM20, HEM20Sn, and HEM40Sn ceramics measured in an argon atmosphere from 25 to 1200 °C.

HEM20Sn and HEM40Sn. These findings indicate that the addition of Sn has a minimal effect on the bond strength. This conclusion is supported by the similar cohesion energy results obtained from DFT calculations for all three samples, which are −7.116, −7.0695, and −7.0757 eV/atom for HEM20, HEM20Sn, and HEM40Sn, respectively. While secondary factors such as variations in grain size and defects influence thermal expansion, these are not intrinsic factors.

Figure 6(a) shows the thermal diffusivity of the HEM20, HEM20Sn, and HEM40Sn samples as a function of temperature, with values of 3.09, 5.43, and 3.71 mm^2/s at room temperature, respectively. These values are significantly lower than those of single-phase MAX materials, such as Ti_2AlC (10.50 mm^2/s) [54]. The decrease in thermal diffusivity is due mainly to enhanced phonon scattering, a common thermal behavior in high-entropy materials, caused by the solid solution of atoms of different sizes and the resulting significant lattice distortions. These distortions, along with the fine grain sizes of high-entropy materials, greatly increase phonon scattering, further lowering the thermal diffusivity. In the case of HEM20, the smallest grain size (4 μm in length and 2 μm in width) results in the lowest thermal diffusivity, as the high density of grain boundaries hinders phonon transport.

In contrast, the larger grain sizes in HEM20Sn and HEM40Sn lead to higher thermal diffusivity values because of reduced grain boundary scattering. Compared with HEM20Sn, HEM40Sn has a lower thermal diffusivity, which can be attributed to the higher Hf content at the M-site. The increased disparity in the atomic radii results in greater lattice distortion, leading to enhanced phonon scattering, which is consistent with the established trend that larger atomic radius differences cause more severe phonon dispersion. As the temperature increases to 1200 °C, the thermal diffusivity of all three samples converges, indicating that the phonon scattering mechanism becomes more dominant. This convergence suggests that lattice vibrations increase with temperature.

Figure 6(b) shows the variation in c_p for the three high-entropy MAX phases between 25 and 1200 °C in a helium environment. At room temperature, the heat capacities of HEM20, HEM20Sn, and HEM40Sn are 0.37, 0.32, and 0.32 J/(g·K), respectively, and they increase with temperature. By 1200 °C, these values increase to 0.61, 0.49, and 0.52 J/(g·K), respectively. The effect of Sn on the thermal capacity is mainly observed in the high-temperature phase, where phonons have a greater influence than does the thermal capacity. Additionally, in this phase, phonons contribute more significantly to the overall effect. As the temperature exceeds 1000 °C, the heat capacity curves of HEM20Sn and HEM40Sn flatten, approaching the Dulong–Petit limit, indicating the stabilization of lattice vibrations at higher temperatures. The specific heat capacity is closely related to the Debye temperature, which can be estimated from elastic constants such as the bulk modulus, shear modulus, and density of the material. The partial substitution of Sn for aluminum in a solid solution at the A-site results in an increase in the bulk modulus and a reduction in the

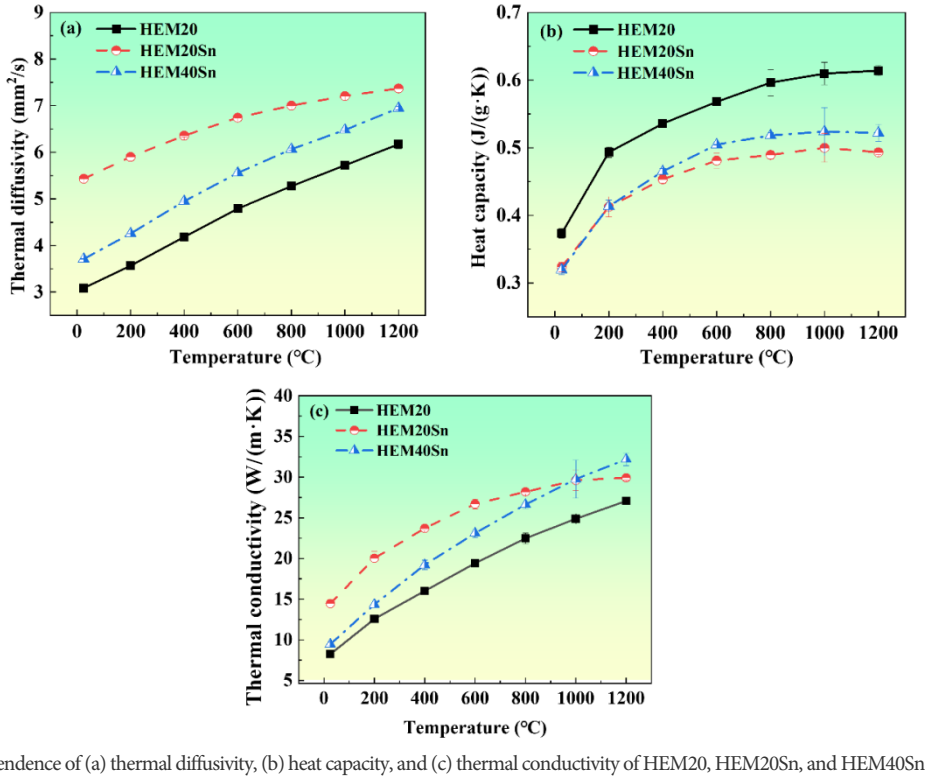

Fig. 6 Temperature dependence of (a) thermal diffusivity, (b) heat capacity, and (c) thermal conductivity of HEM20, HEM20Sn, and HEM40Sn ceramics is measured in a helium atmosphere from 25 to 1200 °C.

shear modulus, which in turn affects the Debye temperature. The stabilization of the heat capacity in the Sn-containing samples also suggests that the Debye temperature plays a critical role in controlling the thermal behavior, a characteristic influenced by changes in the sound velocity and modulus caused by Sn substitution. The slightly higher heat capacity of HEM40Sn than of HEM20Sn is likely due to the greater number of defects induced by the equimolar solid solution at the M-site, which increases c_p.

Figure 6(c) presents the thermal conductivity of the high-entropy MAX phases. At room temperature, the thermal conductivity of HEM20, HEM20Sn, and HEM40Sn ranges from 8.24 to 14.49 W/(m·K), which is significantly lower than that of single-component MAX phases such as Ti_2AlC (27.0 W/(m·K)). As the temperature increases, the thermal conductivity of HEM40Sn increases sharply, eventually matching that of HEM20Sn at approximately 1000 °C. This increase is likely due to the increased phonon thermal conductivity in HEM40Sn, driven by atomic-scale disorder at the M-site. This disorder increases the material's susceptibility to thermal vibrations and heat transfer. The lowest thermal conductivity is observed for HEM20, which may be attributed to its higher grain boundary density. At elevated temperatures, the thermal conductivity of HEM40Sn is slightly greater than that of HEM20Sn, which may be related to its greater cohesive energy, indicating a more stable crystal structure at higher temperatures. Since thermal conductivity is predominantly influenced by lattice vibration during the high-temperature phase, reduced phonon scattering may be the underlying cause of the slightly elevated thermal conductivity. Additionally, thermal conductivity is affected by a multitude of factors, including lattice distortion, defects, and composition. These factors may lead to enhanced phonon scattering, which, in turn, impacts the thermal conductivity performance.

The above results indicate that although the thermal conductivity and thermal diffusion coefficient of the material can be effectively reduced by MAX-phase high-entropy engineering, which has significant advantages over single-phase materials, the effect of high grain boundary density should not be neglected. For example, in the HEM20 ceramics, high-density grain boundaries have an important influence on the thermal properties, and a high grain boundary density hinders the heat conduction path, leading to a further reduction in the thermal conductivity. Therefore, a variety of factors need to be considered when regulating the thermal properties of high-entropy MAX-phase material.

3.4 Mechanical properties

Owing to significant lattice distortion, high-entropy materials typically exhibits greater strength and hardness than single-phase material do. This phenomenon has been confirmed in various high-entropy compounds. Studies based on first principles indicate that a partial solid solution of Sn at the A site can increase the bulk modulus and decrease the shear modulus [56]. Furthermore, a similar trend in mechanical property changes has been observed with increasing valence electron concentration (VEC) [44]. In high-entropy MAX-phase materials, it is anticipated that precise regulation of mechanical properties can be achieved by adjusting the Sn content. Consequently, the effects of Sn on the mechanical properties of these materials are examined in detail in this section.

At a 9.8 N load, the hardness values for HEM20, HEM20Sn, and HEM40Sn are 12.22, 6.98, and 6.61 GPa, respectively, which are significantly higher than those reported for single-phase MAX phases. HEM20 has a markedly greater hardness than single-phase MAX phases do, which is consistent with the established ability of high-entropy materials to exhibit increased hardness due to lattice distortion and a high grain boundary density [57]. The addition of Sn has been shown to significantly reduce the hardness of the system, following the established trend of Sn leading to a decrease in the shear modulus (G). However, the hardness profiles of HEM20Sn and HEM40Sn are similar, indicating that the A-site element strongly influences the modulus. HEM40Sn has a slightly lower hardness than HEM20Sn does, which may be related to the

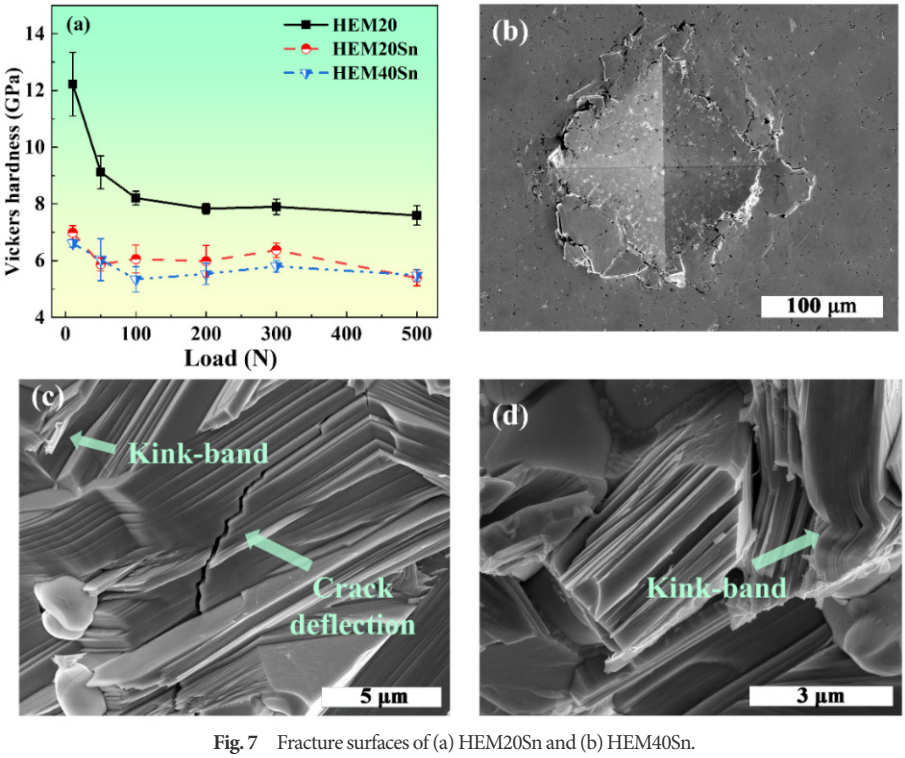

Fig. 7 Fracture surfaces of (a) HEM20Sn and (b) HEM40Sn.

greater densification of HEM20Sn. Figure S9 in the ESM indicates the absence of crack extension in samples. SEM analysis revealed no cracks along the diagonal of the indentations, with grain extrusion and delamination identified as the primary damage mechanisms, suggesting high damage tolerance in these materials.

The fracture surfaces in Figs. 7(a) and 7(b) exhibit layered grains, crack deflection, and distinct kink-band structures, which are characteristic features of MAX phases. These kink-bands facilitate interlayer slip, enhancing the plastic deformation capabilities of high-entropy MAX phases. The substitution of Sn for Al increases the bulk modulus while reducing the shear modulus, leading to a lower hardness in HEM20Sn and HEM40Sn than in HEM20. Furthermore, the addition of Sn enhances ductility, as indicated by the presence of kink bands in Figs. 7(a) and 7(b). These structures, observed at multiple length scales, contribute to the dissipation of mechanical energy, improving toughness and mechanical damping—an exceptional combination in these materials. The substitution of Sn also increases the Poisson's ratio and reduces the G/B ratio, further confirming the transition toward greater ductility.

Table 3 presents the fundamental mechanical and physical properties of the high-entropy MAX phases. Notably, the addition of Sn not only preserves the characteristic low thermal conductivity of high-entropy materials but also maintains their strong mechanical performance. For example, HEM20Sn exhibited the highest bending strength at 500 MPa, demonstrating that adding Sn did not compromise the strength. Moreover, HEM20 retains the highest compressive strength at 1079 MPa and the highest fracture toughness at 7.31 MPa·m$^{1/2}$. High-entropy MAX phases outperform single-phase MAX phases in both flexural strength and compressive strength. This can be attributed to the substantial lattice distortion induced by multielement solid solutions, which is particularly significant in terms of the M-site composition. The multielement configuration enhances strength and stability without diminishing material properties due to Sn substitution. Both HEM20Sn and HEM40Sn maintain excellent mechanical properties, demonstrating that the addition of Sn does not degrade but rather complements the inherent strengths of high-entropy MAX materials. These findings align with theoretical predictions, reinforcing the potential of high-entropy MAX phases for advanced applications that require a combination of high hardness and toughness.

Table 3 Typical physical and mechanical properties of HEM20, HEM20Sn, and HEM40Sn ceramics

Property	HEM20	HEM20Sn	HEM40Sn	Ti_2AlC [53]
Density (g/cm^3) (relative density)	7.14 (97.67%)	8.23 (99.87%)	8.56 (96.07%)	4.11
Mean grain size (μm)	4.36 (*L*), 2.00 (*W*)	15.92 (*L*), 4.55 (*W*)	12.28 (*L*), 3.60 (*W*)	20.0 (*L*), 5.0 (*W*)
Thermal expansion coefficient (10^{-6} K^{-1})	9.46	9.08	9.54	8.20
Thermal diffusivity (mm^2/s) (25 °C)	3.09	5.43	3.71	10.50
Heat capacity, c_p (J/(g·K)) (25 °C)	0.37	0.32	0.32	0.58
Thermal conductivity (W/(m·K)) (25 °C)	8.24	14.49	9.65	27.00
Vickers hardness (GPa) (9.8 N)	12.22±1.22	6.98±0.25	6.61±0.13	4.20
Flexural strength (MPa)	457.91±16.46	500.55±19.97	456.88±24.56	384
Fracture toughness (MPa·m$^{1/2}$)	7.31±0.66	6.71±0.86	5.74±0.82	7
Compressive strength (MPa)	1079±82.43	1020.21±27.27	990.58±85.02	670

Note: *L* refers to the length, and *W* refers to the width.

4 Conclusions

In this study, we present a method for the stable synthesis of single-phase high-entropy MAX-phase bulk using the low-melting-point metal tin, detailing the mechanism behind this strategy. We examined the impact of this method on the physical and mechanical properties of the high-entropy MAX phase and confirmed that it does not compromise the fundamental properties of the high-entropy MAX phase as a structural ceramic.

(1) The addition of Sn, a low-melting-point metal, promotes elemental diffusion. First-principles calculations revealed that the incorporation of Sn improved the thermodynamic stability of the high-entropy MAX phase, as indicated by increases in both the enthalpy of formation and cohesion energy. Moreover, the addition of Sn led to a slight decrease in the mixing enthalpy, resulting in a value closer to zero. This change helps reduce the Gibbs free energy and supports the formation of a homogeneous solid solution of the elements. Moreover, tin exhibits stronger covalent bonding than aluminum does, which further contributes to the stability of the single-phase MAX structure.

(2) The incorporation of an Sn solid solution at the A-site leads to a significant expansion of the lattice constant, which is driven by interactions with various transition metal elements at the M-site. Both theoretical calculations and experimental evidence support this phenomenon. The increased cell volume accommodates larger atoms in the solid solution and enhances the distortion of the octahedral M_6X and trigonal M_6A structural units. This effectively releases the distortion elastic energy of the lattice, which stabilizes the crystal structure of the high-entropy MAX phase and helps prevent phase separation.

(3) The high-entropy MAX phases synthesized with Sn maintain the unique characteristics of high-entropy materials. They exhibit bending strength of 450–500 MPa, compressive strength of 990–1020 MPa, and fracture toughness values ranging from 5.74 to 6.71 MPa·m$^{1/2}$. The hardness values fall between 6.61 and 6.98 GPa, whereas the thermal conductivity ranges from 8.24 to 14.49 W/(m·K). These properties emphasize their significant potential for application as structural materials.

We believe that this approach shows potential for investigating other novel formulations of single-phase high-entropy 211 MAX materials, serving as a promising research direction in the field of structural materials.

Acknowledgements

This work was supported by the National Natural Sciences Foundation of China (Nos. 52072311 and 52472079) and Sichuan Science and Technology Program (2025YFHZ0082).

Declaration of competing interest

The authors have no competing interests to declare that are relevant to the content of this article. The author Yanchun Zhou is

the Editors-in-Chief of this journal. The author Chunfeng Hu is the Editorial Committee member of this journal.

Electronic Supplementary Material

Supplementary material is available in the online version of this article at https://doi.org/10.26599/JAC.2025.9221028.

References

[1] Yeh JW, Chen SK, Lin SJ, *et al.* Nanostructured high-entropy alloys with multiple principal elements: Novel alloy design concepts and outcomes. *Adv Eng Mater* 2004, **6**: 299–303.

[2] Cantor B, Chang ITH, Knight P, *et al.* Microstructural development in equiatomic multicomponent alloys. *Mat Sci Eng A-Struct* 2004, **375–377**: 213–218.

[3] Zhang WT, Wang XQ, Zhang FQ, *et al.* Frontiers in high entropy alloys and high entropy functional materials. *Rare Metals* 2024, **43**: 4639–4776.

[4] Rost CM, Sachet E, Borman T, *et al.* Entropy-stabilized oxides. *Nat Commun* 2015, **6**: 8485.

[5] Sarker P, Harrington T, Toher C, *et al.* High-entropy high-hardness metal carbides discovered by entropy descriptors. *Nat Commun* 2018, **9**: 4980.

[6] Feng L, Fahrenholtz WG, Hilmas GE, *et al.* Synthesis of single-phase high-entropy carbide powders. *Scripta Mater* 2019, **162**: 90–93.

[7] Mizutani U. Hume-Rothery rules for structurally complex alloy phases. *MRS Bull* 2012, **37**: 169.

[8] Zhang Y, Zhou YJ, Lin JP, *et al.* Solid-solution phase formation rules for multi-component alloys. *Adv Eng Mater* 2008, **10**: 534–538.

[9] Yang SG, Lu J, Xing FZ, *et al.* Revisit the VEC rule in high entropy alloys (HEAs) with high-throughput CALPHAD approach and its applications for material design-a case study with Al–Co–Cr–Fe–Ni system. *Acta Mater* 2020, **192**: 11–19.

[10] Ye YF, Liu CT, Yang Y. A geometric model for intrinsic residual strain and phase stability in high entropy alloys. *Acta Mater* 2015, **94**: 152–161.

[11] Zhang FX, Tong Y, Jin K, *et al.* Lattice distortion and phase stability of Pd-doped NiCoFeCr solid-solution alloys. *Entropy* 2018, **20**: 900.

[12] Sokol M, Natu V, Kota S, *et al.* On the chemical diversity of the MAX phases. *Trends Chem* 2019, **1**: 210–223.

[13] Zhang Z, Duan XM, Jia DC, *et al.* On the formation mechanisms and properties of MAX phases: A review. *J Eur Ceram Soc* 2021, **41**: 3851–3878.

[14] Du CF, Xue YQ, Wang CC, *et al.* Synthesis of a high-entropy $(TiVCrMo)_3AlC_2$ MAX and its tribological properties in a wide temperature range. *J Eur Ceram Soc* 2023, **43**: 4684–4695.

[15] Zhou J, Tao QZ, Ahmed B, *et al.* High-entropy laminate metal carbide (MAX phase) and its two-dimensional derivative MXene. *Chem Mater* 2022, **34**: 2098–2106.

[16] Du ZG, Wu C, Chen YC, *et al.* High-entropy carbonitride MAX phases and their derivative MXenes. *Adv Energy Mater* 2022, **12**: 2103228.

[17] Qiao LJ, Bi JQ, Liang GD, *et al.* Synthesis and electromagnetic wave absorption performances of a novel $(Mo_{0.25}Cr_{0.25}Ti_{0.25}V_{0.25})_3AlC_2$ high-entropy MAX phase. *J Mater Sci Technol* 2023, **137**: 112–122.

[18] Leong Z, Jin HM, Wong ZM, *et al.* Elucidating the chemical order and disorder in high-entropy MXenes: A high-throughput survey of the atomic configurations in $TiVNbMoC_3$ and $TiVCrMoC_3$. *Chem Mater* 2022, **34**: 9062–9071.

[19] Seong HW, Lee MS, Ryu HJ. First-principles study for discovery of novel synthesizable 2D high-entropy transition metal carbides (MXenes). *J Mater Chem A* 2023, **11**: 5681–5695.

[20] Liu C, Yang YY, Zhou ZF, *et al.* $(Ti_{0.2}V_{0.2}Cr_{0.2}Nb_{0.2}Ta_{0.2})_2AlC$–$(Ti_{0.2}V_{0.2}Cr_{0.2}Nb_{0.2}Ta_{0.2})C$ high-entropy ceramics with low thermal conductivity. *J Am Ceram Soc* 2022, **105**: 2764–2771.

[21] Zou HR, Zhang JY, Ren L, *et al.* Microstructure mechanical properties and tribological properties of high entropy M_2AlC-MC (M = Ti, V, Zr, Hf, Ta) composites prepared via spark plasma sintering. *J Eur Ceram Soc* 2024, **44**: 1421–1428.

[22] Cao L, Zhang QQ, Du LJ, *et al.* Synthesis and characterization of high entropy $(TiVNbTaM)_2AlC$ (M = Zr, Hf) ceramics. *J Adv Ceram* 2024, **13**: 237–246.

[23] Si JJ, Yu JQ, Lan HH, *et al.* Chemical potential-modulated ultrahigh-phase-purity growth of ultrathin transition-metal boride single crystals. *J Am Chem Soc* 2023, **145**: 3994–4002.

[24] Chen YX, Liu KL, Liu JX, *et al.* Growth of 2D GaN single crystals on liquid metals. *J Am Chem Soc* 2018, **140**: 16392–16395.

[25] Cao GH, Liang JJ, Guo ZL, *et al.* Liquid metal for high-entropy alloy nanoparticles synthesis. *Nature* 2023, **619**: 73–77.

[26] He QF, Wang JG, Chen HA, *et al.* A highly distorted ultraelastic chemically complex Elinvar alloy. *Nature* 2022, **602**: 251–257.

[27] Hug G, Jaouen M, Barsoum MW. X-ray absorption spectroscopy, EELS, and full-potential augmented plane wave study of the electronic structure of Ti_2AlC, Ti_2AlN, Nb_2AlC, and $(Ti_{0.5}Nb_{0.5})_2AlC$. *Phys Rev B* 2005, **71**: 024105.

[28] Bai DL, Wang Q, Deng B, *et al.* Liquid metal assistant self-propagating high-temperature synthesis of S-containing high-entropy MAX-phase materials. *J Mater Sci Technol* 2025, **209**: 1–8.

[29] Zhang H, Hu T, Wang XH, *et al.* Discovery of carbon-vacancy ordering in Nb_4AlC_{3-x} under the guidance of first-principles calculations. *Sci Rep-UK* 2015, **5**: 14192.

[30] Kresse G, Furthmüller J. Efficiency of *ab-initio* total energy calculations for metals and semiconductors using a plane-wave basis set. *Comp Mater Sci* 1996, **6**: 15–50.

[31] van de Walle A, Tiwary P, de Jong M, *et al.* Efficient stochastic generation of special quasirandom structures. *Calphad* 2013, **42**: 13–18.

[32] Perdew JP, Burke K, Ernzerhof M. Generalized gradient approximation made simple. *Phys Rev Lett* 1996, **77**: 3865–3868.

[33] Kresse G, Joubert D. From ultrasoft pseudopotentials to the projector augmented-wave method. *Phys Rev B* 1999, **59**: 1758–1775.

[34] Wang V, Xu N, Liu JC, *et al.* VASPKIT: A user-friendly interface facilitating high-throughput computing and analysis using VASP code. *Comp Mater Sci* 2021, **267**: 108033.

[35] Momma K, Izumi F. VESTA 3 for three-dimensional visualization of crystal, volumetric and morphology data. *J Appl Crystallogr* 2011, **44**: 1272–1276.

[36] Becke AD, Edgecombe KE. A simple measure of electron localization in atomic and molecular systems. *J Chem Phys* 1990, **92**: 5397–5403.

[37] Slater JC. Atomic radii in crystals. *J Chem Phys* 1964, **41**: 3199–3204.

[38] Dahlqvist M, Barsoum MW, Rosen J. MAX phases—Past, present, and future. *Mater Today* 2024, **72**: 1–24.

[39] Cai LP, Huang ZY, Hu WQ, *et al.* Fabrication and microstructure of a new ternary solid solution of $Ti_3Al_{0.8}Si_{0.2}Sn_{0.2}C_2$ with high solid solution strengthening effect. *Ceram Int* 2018, **44**: 9593–9600.

[40] Tian ZH, Zhang PG, Sun WW, *et al.* Vegard's law deviating $Ti_2(Sn_xAl_{1-x})C$ solid solution with enhanced properties. *J Adv Ceram* 2023, **12**: 1655–1669.

[41] Ye BL, Wen TQ, Nguyen MC, *et al.* First-principles study, fabrication and characterization of $(Zr_{0.25}Nb_{0.25}Ti_{0.25}V_{0.25})C$ high-entropy ceramics. *Acta Mater* 2019, **170**: 15–23.

[42] Ye BL, Wen TQ, Nguyen MC, *et al.* First-principles study, fabrication, and characterization of $(Hf_{0.2}Zr_{0.2}Ta_{0.2}Nb_{0.2}Ti_{0.2})C$ high-entropy ceramic. *J Am Ceram Soc* 2019, **102**: 4344–4352

[43] Ali M, Yousaf M, Murtaza G, *et al.* Physical properties and defect processes of Zr_3AC_2 (A = Al and Si) MAX phases: Implication for radiation tolerance. *Mater Sci Eng B-Adv* 2024, **308**: 117619.

[44] Hadi MA, Kelaidis N, Filippatos PP, *et al.* Optical response, lithiation and charge transfer in Sn-based 211 MAX phases with electron localization function. *J Mater Res Technol* 2022, **18**: 2470–2479.

[45] Guo S, Liu CT. Phase stability in high entropy alloys: Formation of

solid-solution phase or amorphous phase. *Prog Nat Sci-Mater* 2011, **21**: 433–446.

[46] Zhou YC, Xiang HM, Hu CF. Extension of MAX phases from ternary carbides and nitrides (X = C and N) to ternary borides (X = B, C, and N): A general guideline. *Int J Appl Ceram Tec* 2023, **20**: 803–822.

[47] Yeh JW, Chang SY, Hong YD, *et al.* Anomalous decrease in X-ray diffraction intensities of Cu–Ni–Al–Co–Cr–Fe–Si alloy systems with multi-principal elements. *Mater Chem Phys* 2007, **103**: 41–46.

[48] Lapauw T, Tunca B, Potashnikov D, *et al.* The double solid solution $(Zr,Nb)_2(Al,Sn)C$ MAX phase: A steric stability approach. *Sci Rep-UK* 2018, **8**: 12801.

[49] Tunca B, Lapauw T, Delville R, *et al.* Synthesis and characterization of double solid solution $(Zr,Ti)_2(Al,Sn)C$ MAX phase ceramics. *Inorg Chem* 2019, **58**: 6669–6683.

[50] Kanoun MB, Goumri-Said S, Reshak AH. Theoretical study of mechanical, electronic, chemical bonding and optical properties of Ti_2SnC, Zr_2SnC, Hf_2SnC and Nb_2SnC. *Comp Mater Sci* 2009, **47**: 491–500.

[51] Ma K, Shi XG, He GQ, *et al. In situ* reaction synthesis, microstructure and thermomechanical properties of novel medium-entropy $(Ti,V,Nb,Ta)_2AlC$ ceramics. *Ceram Int* 2023, **49**: 21206–21212.

[52] He GQ, Zhang Y, Yao P, *et al.* A novel medium-entropy $(TiVNb)_2AlC$ MAX phase: Fabrication, microstructure, and properties. *J Mater Sci Technol* 2023, **137**: 91–99.

[53] Wang XH, Zhou YC. Solid–liquid reaction synthesis and simultaneous densification of polycrystalline Ti_2AlC. *Int J Mater Res* 2002, **93**: 66–71.

[54] Zhou WB, Li K, Zhu JQ, *et al.* Rapid synthesis of highly pure Nb_2AlC using the spark plasma sintering technique. *J Phys Chem Solids* 2018, **120**: 218–222.

[55] Hu CF, He LF, Zhang J, *et al.* Microstructure and properties of bulk Ta_2AlC ceramic synthesized by an *in situ* reaction/hot pressing method. *J Eur Ceram Soc* 2008, **28**: 1679–1685.

[56] Ali MA, Hossain MM, Jahan N, *et al.* Newly synthesized Zr_2AlC, $Zr_2(Al_{0.58}Bi_{0.42})C$, $Zr_2(Al_{0.2}Sn_{0.8})C$, and $Zr_2(Al_{0.3}Sb_{0.7})C$ MAX phases: A DFT based first-principles study. *Comp Mater Sci* 2017, **131**: 139–145.

[57] Han Y, Liu XY, Zhang QQ, *et al.* Ultra-dense dislocations stabilized in high entropy oxide ceramics. *Nat Commun* 2022, **13**: 2871.